

RADARGRAMMETRY WITH CHANDRAYAAN-1 AND LRO MINI-RF IMAGES OF THE MOON

R.L. Kirk^{a,*}, D.A. Cook^a, E. Howington-Kraus^a, J.M. Barrett^a, T.L. Becker^a, C.D. Neish^b, B.J. Thomson^b, D.B.J. Bussey^b

^a Astrogeology Science Center, U.S. Geological Survey, Flagstaff, AZ 86001 USA –
(rkirk, dcook, ahowington, jbarrett, tbecker)@usgs.gov

^b JHU Applied Physics Laboratory, Laurel, MD 20723 USA –
(catherine.neish, bradley.thomson, ben.bussey)@jhuapl.edu

Commission IV, WG IV/7

KEY WORDS: planetary mapping, radargrammetry, lunar, triangulation, DTM

ABSTRACT:

The Mini-RF investigation consists of polarimetric synthetic aperture radar (SAR) imagers on the ISRO Chandrayaan-1 lunar orbiter and the NASA Lunar Reconnaissance Orbiter (LRO), with the primary objective of searching for water ice in permanent shadows at the lunar poles. We describe the software and techniques we have developed for radargrammetric analysis of the Mini-RF images, which enable us to make controlled image mosaics with relative and absolute positional accuracy an order of magnitude better than uncontrolled products, as well as digital topographic models (DTMs), and orthoimages. A primary motivation for such processing is to coregister the radar images as closely as possible to one another and to other datasets, so that detailed analyses (e.g., of putative ice deposits and of the LCROSS impact site) can be made.

Bundle adjustment and orthorectification have been implemented in the USGS cartographic software package ISIS and will be available to the research community in the near future. DTM production relies on the commercial stereo analysis software SOCET SET (® BAE Systems), with a rigorous sensor model written by us; images and metadata are prepared in ISIS. The resolution and vertical precision of the Mini-RF DTMs depend on the image resolution and convergence geometry. For images in zoom-mode (7.5 m/pixel, used for the majority of observations) viewing the site from opposing directions, a vertical precision of ~10 m and horizontal resolution of 50–200 m has been achieved. The zoom mode data, with intermediate resolution between those of the LROC narrow-angle and wide-angle cameras, are also well suited for completing a uniform global topographic model of the Moon by filling in km-scale gaps between LOLA altimetry tracks in the equatorial zone with controlled stereo DTMs.

1. INTRODUCTION

The first decade of the twenty-first century has seen a rebirth of interest in lunar exploration, with Europe, Japan, China, India, and the United States all launching lunar missions (Kirk et al., 2008a). A key objective of several of these missions has been to investigate the possible presence of water ice in permanently shadowed areas near the lunar poles (Nozette et al., 1996; 1997; Bussey et al. 2003; but see also Campbell et al., 2006). As a result, a pair of Synthetic Aperture Radar (SAR) imagers was selected for flight on the Indian Chandrayaan-1 and US Lunar Reconnaissance Orbiter (LRO) probes. Known collectively as the Miniature Radio Frequency experiment (Mini-RF; Nozette et al., 2010), these instruments not only “see in the dark” by providing their own illumination in order to produce the first shadow-free images of the lunar poles, they also measure the full polarization characteristics of the reflected signal for circularly polarized transmitted radiation (Raney, 2007). A strong return in the “unexpected” (i.e., not reversed as it would be if reflected from a smooth interface) sense of circular polarization can be indicative of radar-transparent materials such as ice (e.g., Harmon et al., 2001) although diffuse scattering from rough surfaces such as fresh, blocky impact crater ejecta can also produce a similar polarization signal.

Taking full advantage of this new ability to see into the shadows and even into the shallow subsurface and even into the shallow subsurface of the Moon requires new tools for radargrammetry.

These are analogous to the more familiar methods of photogrammetry but take into account the geometric principles by which SAR images are formed. In this paper we describe the software and techniques we have developed for radargrammetric analysis of the Mini-RF images, enabling us to make controlled image mosaics with precision and accuracy improved by at least an order of magnitude compared to uncontrolled products, as well as digital topographic models (DTMs), from which orthoimages (images from which topographic parallax distortions have been removed), slope maps, and other products can be generated. A primary motivation for both types of processing is to coregister the radar images as closely as possible to one another and to other datasets (Archinal et al., 2010), so that detailed analyses can be made. Targets of particular interest for such studies include candidate ice-rich craters (Thomson et al., 2010), pyroclastic deposits (Carter et al., 2010; Trang et al., 2010), and the impact site of the Lunar Crater Reconnaissance and Observation Sensing Satellite (LCROSS; Colaprete et al., 2009; Neish et al., 2010), mapping of which is discussed below.

2. MISSIONS AND DATA

2.1 Chandrayaan-1

The Indian Space Research Organization (ISRO) Chandrayaan-1 probe was launched on 22 October 2008 and entered lunar

* Corresponding author.

orbit on 8 November, reaching its 100-km circular mapping orbit four days later. A two-year mapping mission at this altitude was originally planned, but difficulties in maintaining thermal control of the spacecraft led to the orbit being raised to 200 km on 19 May 2009. Contact with the spacecraft was lost on 29 August 2009, ending the mission after 312 days. One of the 11 instruments onboard Chandrayaan-1 was the US-provided Mini-SAR, also known as “Forerunner” (i.e., of the subsequent and more capable LRO Mini-RF instrument). Mini-SAR operated at a wavelength of 12.6 cm (S band), obtaining images at a resolution of 150 m (processed on the ground at 75 m/pixel) with a swath width of 13 km and a nominal incidence angle near 33° (varying by $\pm 2.5^\circ$ across the swath). Between February and April 2009, Mini-SAR used this mode to image >95% of the areas poleward of 80° N and S (Figure 1; Spudis et al., 2009). A total of 15 non-polar targets were also imaged, in part to provide a point of comparison for polar features. The polar orbit of the spacecraft, combined with the side-looking geometry required for SAR imaging, resulted in small gaps near the poles themselves. Mini-SAR was therefore designed to obtain lower resolution (1x10 km) scatterometry observations when the spacecraft was rotated to point its antenna directly below the flight track, filling the SAR gap. Unfortunately, no observations were taken in this mode prior to the end of the mission.

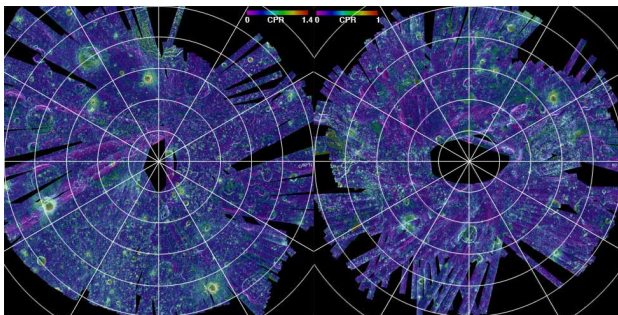


Figure 1. Mosaics of Chandrayaan-1 Mini-SAR images of the north (left) and south (right) poles of the Moon, obtained in February–April 2009. Image intensity is derived from total received power, color encodes circular polarization ratio. Polar Stereographic projections from 80° to the pole. Grid spacing is 30° in longitude, 20° in latitude.

2.2 Lunar Reconnaissance Orbiter

NASA launched LRO and LCROSS on a single Atlas V vehicle on 18 June 2009. LRO entered an elliptical lunar orbit on 23 June, and reached its 50-km circular mapping orbit on 15 September. As of this writing, the spacecraft is still operating successfully in this orbit and is about to complete its one-year mapping mission. Various options for an extended science mission lasting one to two years (including a transition to one or more higher, more stable orbits) are being considered. Meanwhile, LCROSS impacted the permanently shadowed interior of the crater Cabeus near the Moon’s south pole on 9 October 2009. Despite having the status of a “technology demonstration” and originally being allocated only a few minutes observing time per month, the LRO Mini-RF is considerably more capable than Forerunner. It can operate at either 12.6 or 4.2 cm wavelength. The latter is formally C-band but is usually referred to as “X-band” mode for historical reasons. At both wavelengths a baseline SAR mode similar to that of Forerunner and a zoom mode with 15-m (along-track) by 30-m (across-track) resolution are available, the latter being processed at a grid spacing of 7.5 m/pixel. The majority of observations to date have been obtained in S-band zoom mode

because it provides the optimum combination of high resolution with large (~ 18 km) swath width; the X-band swath is only ~ 6 km across. The nominal incidence angle is roughly 48° , varying by $\pm 5^\circ$ across the S-band swath. LRO Mini-RF lacks the scatterometry mode of Mini-SAR but adds an interferometric mode for topographic mapping.

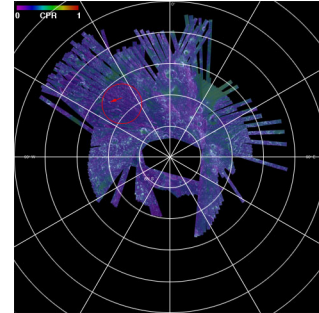


Figure 2. Mosaic of LRO Mini-RF S-zoom images of the south pole of the Moon, obtained in support of the LCROSS mission in June–September 2009. Circle indicates the rim of crater Cabeus, arrow indicates the approximate impact point of LCROSS. Projection and color coding as in Fig. 1.

During its commissioning phase, between June and September 2009, Mini-RF supported the LCROSS mission by obtaining S-zoom images of much of the lunar south polar region, including Cabeus (Figure 2; Neish et al., 2010). The image strips in this sequence generally extend from near the pole to $\sim 85^\circ$ S on either side. As a consequence, key longitudes were imaged both from the east and from the west as the Moon rotated relative to the LRO orbit plane, providing strongly convergent stereo coverage as will be discussed below. Nearly complete S-zoom observations from each pole to 70° latitude (Figure 3) were obtained between June and July 2010, when illumination conditions were unfavorable for LRO’s optical instruments. Full west-looking mosaic of both poles were obtained during June 2010. In early July, the angle β between the orbit plane and sun direction spacecraft passed through 90° , causing the spacecraft to become east-looking, and additional polar mosaics were obtained. Outside of these periods of intensive polar observations near $\beta = 90^\circ$, Mini-RF has been allowed to operate much more often than was originally envisioned, and has imaged a substantial and growing fraction of the Moon’s equatorial zone (Figure 4). All operating modes have been exercised, although the majority of observations have been obtained in S-zoom mode. A targeted S-zoom stereo observation of Jackson crater is of particular importance for our radargrammetric studies and will be described in detail below.

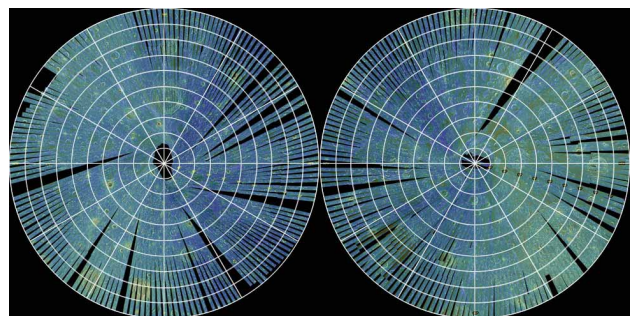


Figure 3. Mosaics of LRO Mini-RF S-zoom images of the north (left) and south (right) poles of the Moon, obtained in June–July 2010. Projection, grid, and color coding as in Fig. 1 except that mosaics extend from 70° to the pole.

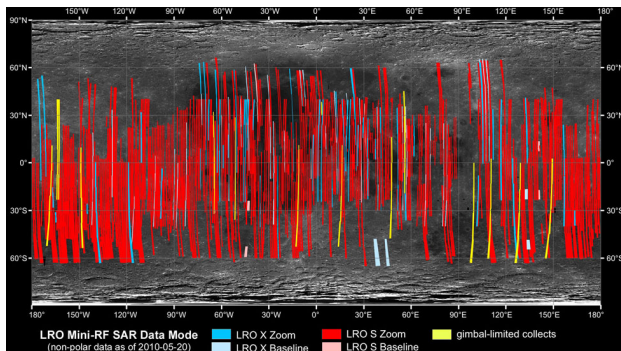


Figure 4. Map showing non-polar images acquired by LRO Mini-RF as of 20 May 2010. Color indicates operating mode and wavelength. Simple Cylindrical projection covering the whole Moon, centered at 0° latitude and longitude.

2.3 Source Data Processing and Formats

The initial processing of the Chandrayaan-1 and LRO Mini-RF data is performed by the Vexcel Corporation, using software with an extensive heritage from Earth applications. Intermediate processing is carried out by the Mini-RF team at the Applied Physics Laboratory, using the digital cartographic software ISIS (Integrated Software for Imagers and Spectrometers) developed by the U.S. Geological Survey (Anderson et al., 2004; <http://isis.astrogeology.usgs.gov>). The steps in this processing chain result in a series of distinct data products that correspond to the levels of cartographic processing described by Batson (1990). The Level 0 product records the signal received by the instrument in non-image form. The first viewable image, the Level 1 product, is formed by processing Level 0 data with a SAR correlation algorithm. The pixel spacing of the Level 1 images can be selected as a parameter of the SAR processor. The Mini-RF images are processed at 75 m/pixel (baseline mode) or 7.5 m/pixel (zoom mode) to ensure that the intrinsic resolution of the instrument is oversampled. Pixel coordinates in a Level 1 image are not georeferenced, but instead reflect the geometry of the SAR imaging process, as described in detail below. For now, we note that the Level 1 SAR image resembles an image from an optical pushbroom scanner in that each image line corresponds to a particular time during image formation and contains only the features in a given plane through the spacecraft at that time. Where SAR and pushbroom images differ lies in how the cross-track coordinates in a given line are determined: based on range in the former or on angle in the latter. The hybrid polarity design of Mini-RF (Raney, 2007) leads to a multi-band image with four observed values at each pixel (intensity in the horizontal and vertical linearly polarized modes, and the real and imaginary parts of the cross-product between these modes). As archived in the NASA Planetary Data System (PDS), each Level 1 product consists of a binary file containing the four-band image in band interleaved by pixel (BIP) order, a text file containing a detached PDS label, and a second text file containing the Vexcel processing label from which the PDS label information was derived (Reid, 2009). These Level 1 products are the main inputs for our radargrammetric analyses.

Level 2 products are individual images that have been map-projected, and Level 3 products are mosaics of such images. The standard products at these levels are uncontrolled, and are (so far) projected onto the lunar reference sphere, although the Vexcel software is capable of orthorectifying images based on a DTM. We do not make use of these products as inputs, but our analysis generates controlled and orthorectified equivalents as well as detailed local DTMs, so a brief description of these

products is appropriate. The projections and grid spacings used for Levels 2 and 3 are still somewhat in flux, but equatorial products are generally in Equirectangular projection, polar Level 2 images in an Oblique Cylindrical projection that minimizes wasted space by closely approximating the Level 1 geometry, and polar mosaics in Polar Stereographic projection. Scales are normally chosen to give a power of 2 pixels per degree (Batson, 1990) and either to oversample or (to save data volume) slightly undersample the instrument resolution. In addition to the four observed intensities in a single BIP-ordered file, Level 2 products include the four components of the Stokes vector (Campbell, 2002, pp. 25–28) in separate files and “daughter products” consisting of the same-sense and opposite-sense circularly polarized intensities and the ratio of these or circular polarization ratio (CPR). Uncontrolled Level 3 products have been produced for use within the Mini-RF team but have not yet been archived. Plans call for mosaicking the total received power (first Stokes vector component S_1) and the CPR, likely after normalization to a model backscatter function (Thompson et al., 2010) to reduce variations that are due solely to the incidence angle. Figures 1–3 illustrate how such mosaics might be combined to show both the total backscatter cross-section and polarization.

As of 15 September 2010, LRO Mini-RF data from the period up to 14 June 2010 have been archived in the PDS Geosciences Node and are available at <http://geo.pds.nasa.gov/missions/lro/mrf.htm>. Additional LRO data will be archived at 3-month intervals, and the Chandrayaan-1 Mini-SAR data will ultimately be archived as well. The other key data set needed for radargrammetric analysis is the spacecraft trajectory. Information for LRO is available at <ftp://naif.jpl.nasa.gov/pub/naif/pds/data/lro-l-spice-6-v1.0/> and has an accuracy currently estimated to be on the order of 100 m (Archinal et al., 2010). More accurate LRO trajectory data, and data for Chandrayaan-1, will become available in the future. Spacecraft orientation data are not needed for radargrammetry.

3. SOFTWARE AND METHODS

Our radargrammetric processing of Mini-RF images builds on the approach we have used to produce stereo DTMs from numerous optical sensors and the Magellan and Cassini radar imagers (Howington-Kraus et al., 2002; Kirk and Howington-Kraus, 2008; Kirk et al., 2010). In particular, we use ISIS to ingest and prepare the images and supporting geometric data, and to perform a variety of general image analysis and enhancement tasks. We use a commercial digital photogrammetric workstation running SOCET SET (® BAE Systems) software (Miller and Walker, 1993; 1995) for DTM production by automated matching and for interactive editing of DTMs using its stereo display capability. SOCET SET also provides tools for bundle adjustment of the images prior to DTM collection. Using this commercial system with a given data set requires not only an appropriate sensor model (i.e., software that performs the transformation between pixel coordinates in image space and ground coordinates), but also software to translate the images and supporting information from ISIS to SOCET SET formats.

A key difference between Mini-RF and the Magellan and Cassini SARs is that data from these earlier instruments were produced only in map-projected form. As a result, we used ISIS capabilities for transforming data from one projection to another to make uncontrolled mosaics but did not implement an ISIS sensor model for these missions. Instead, we focused on

topographic mapping in SOCET SET and created sensor models that worked by first “undoing” the map projection to get back to the fundamental radar image coordinates of range and Doppler shift. These sensor models were designed to perform rather complex bookkeeping so they could be used with mosaics of data from multiple orbits (Magellan) or multiple radar beams (Cassini). The availability of Mini-RF data in Level 1 coordinates leads to substantial simplification of the sensor model design. Such availability also motivated us to develop a Mini-RF sensor model for ISIS as well as one for SOCET SET. The resulting capability to project images from Level 1 to Level 2 in ISIS might appear redundant because of the Vexcel-supplied Level 2 products, but is in fact extremely useful because the images can first be controlled by using the ISIS tools for automated and interactive point measurement and for bundle adjustment, and because the images can be orthorectified by projection onto topographic datasets, e.g., from the Lunar Orbiter Laser Altimeter (LOLA; Smith et al. 2010) as these become available. As noted, the standard Level 2 products are uncontrolled and unrectified.

3.1 Sensor Models

In both ISIS and SOCET SET, sensor models are implemented in the C++ language and include both a set of required “housekeeping” routines and the essential code that performs the transformation from pixels to ground coordinates and the reverse. The latter, sometimes referred to as the “math model” for the sensor, is described here.

As already noted, each line of a Mini-RF image corresponds to a unique (and uniformly sampled) time. Thus, the spacecraft position \mathbf{x}_s and velocity \mathbf{v}_s corresponding to a given image line l are calculated as follows

$$t = t_1 + (l-1)\Delta t, \quad (1)$$

$$\mathbf{x}_s = \mathbf{x}_s(t), \quad (2)$$

$$\text{and } \mathbf{v}_s = \mathbf{v}_s(t), \quad (3)$$

where t_1 is the time of line 1 and Δt the interline interval, and the position and time histories $\mathbf{x}_s(t)$ and $\mathbf{v}_s(t)$ are interpolated from the spacecraft trajectory data (provided in the form of a SPICE SPK kernel file; Acton, 1999), which are expressed in the body-fixed rotating frame of the target. In the cross-track direction the quantity that is actually observed is the slant range r between the spacecraft and ground. Because gridding the image uniformly in terms of slant range would distort the shape and relative size of features at different ranges, the Level 1 images are sampled uniformly in apparent ground range r_g , measured from the first sample. A third-order polynomial is used to approximate the relation between r and r_g . Thus, for sample s we have

$$r_g = (s-1)\Delta r_g \quad (4)$$

$$\text{and } r = \sum_{i=0}^3 a_i(t) r_g^i \quad (5)$$

where the coefficients $a_i(t)$ are interpolated from their values $a_i(t_j)$ at a series of reference times t_j . These quantities, calculated by the Vexcel SAR processor software, are recorded in the image labels.

To solve for the ground position \mathbf{x} of the given pixel, we note that it lies at a distance r from \mathbf{x}_s and in a plane passing through \mathbf{x}_s perpendicular to the velocity \mathbf{v}_s , the geometric condition for zero Doppler shift at time t . As in photogrammetry, these two

conditions do not fully specify \mathbf{x} , they only limit it to a one-dimensional locus (in the radar case, a circle centered on the spacecraft). For purposes of the sensor model, we obtain a unique solution by specifying the elevation of the ground point, in terms of its distance R from the center of the target body. Thus, we have the following equations implicitly specifying \mathbf{x} :

$$|\mathbf{x} - \mathbf{x}_s| = r, \quad (6)$$

$$(\mathbf{x} - \mathbf{x}_s) \cdot \mathbf{v}_s = 0, \quad (7)$$

$$|\mathbf{x}| = R. \quad (8)$$

These equations can be solved by representing $\mathbf{x} - \mathbf{x}_s$ in terms of an orthogonal basis of vectors $\hat{\mathbf{v}}$, $\hat{\mathbf{t}}$, and $\hat{\mathbf{u}}$, that point in the direction of the velocity, roughly vertical, and to the side. The component along $\hat{\mathbf{v}}$ is zero because of eq. 7 so we have

$$\mathbf{x} - \mathbf{x}_s = a\hat{\mathbf{v}} + b\hat{\mathbf{u}}, \quad (9)$$

$$\text{where } \hat{\mathbf{v}} = \mathbf{v}_s / |\mathbf{v}_s|, \quad (10)$$

$$\hat{\mathbf{t}} = (\mathbf{x}_s - (\mathbf{x}_s \cdot \hat{\mathbf{v}})\hat{\mathbf{v}}) / |\mathbf{x}_s - (\mathbf{x}_s \cdot \hat{\mathbf{v}})\hat{\mathbf{v}}|, \quad (11)$$

$$\text{and } \hat{\mathbf{u}} = \hat{\mathbf{v}} \times \hat{\mathbf{t}}. \quad (12)$$

Substituting eq. 9 into eq. 6-8 and rearranging, we obtain

$$a = \left(R^2 - r^2 - |\mathbf{x}_s|^2 \right) / 2\mathbf{x}_s \cdot \hat{\mathbf{t}}, \quad (13)$$

$$b = \pm \sqrt{r^2 - a^2}. \quad (14)$$

If $r < a$, there is no real solution, indicating that the surface of radius R is too far from the spacecraft to have been imaged at range r . If $r > a$ there are two solutions, one on either side of the spacecraft. Fortunately, only one of these points at a time is illuminated by the radar system, so the sign can be chosen based on whether the recorded look direction for the image is right (+) or left (-).

If the image is being projected onto a reference sphere of fixed radius R , this completes the image to ground calculation. To orthorectify an image onto a DTM, ISIS selects an initial approximation for R (e.g., the average for the body) and uses eq. 9–14 to estimate the ground point location \mathbf{x} . It then samples the DTM at the latitude and longitude corresponding to \mathbf{x} to obtain a new approximation for R . This calculation is iterated and converges rapidly in practice. It is not guaranteed to produce the desired solution when the surface is so rugged that multiple intersections (i.e., radar foldover) occur.

The ground to image transformation involves calculating the slant range r by eq. 6 and the Doppler shift Δf for a given ground point and observation time:

$$\Delta f = -\frac{2}{\lambda} (\mathbf{x}_s - \mathbf{x}) \cdot \mathbf{v}_s / |\mathbf{x}_s - \mathbf{x}|, \quad (15)$$

where λ is the radar wavelength. To determine the image line on which the feature at \mathbf{x} appears, it is necessary to iteratively adjust the assumed time t until $\Delta f = 0$. This process is directly analogous to the iteration required for optical pushbroom scanners. The slant range is then calculated at the solved-for time and eq. 5 must be solved numerically to determine the ground range. Finally, eq. 1 and 4 are used to determine line and sample from time and ground range, respectively.

The ground to image transformation is used slightly differently within a bundle adjustment calculation. It is necessary to

evaluate the residuals between a ground point and a measured image pixel that is identified with it. Equation 6 is therefore evaluated at the fixed time of that image line and the calculated range is compared to the range for the pixel (eq. 1–5). Similarly, eq. 15 is evaluated at the fixed time and compared with the Doppler shift for pixels on that line, i.e., zero by definition. For the ISIS bundle adjustment program *jigsaw*, the partial derivatives of the residuals with respect to the ground coordinates and the adjustable parameters of the spacecraft trajectory were evaluated analytically. In addition, because *jigsaw* does not currently allow for weighting of image observations, we designed the software to normalize the residuals in terms of the ground range resolution δX and azimuth resolution δY . These are the actual instrument resolution, not the pixel spacing, and are calculated by the SAR processor and recorded in the image labels. The weighting used

$$\sigma_r = 100\delta X \sin(i), \quad (16)$$

$$\text{and } \sigma_{\Delta f} = 100\delta Y \frac{2|v_r|}{\lambda f \cos(i)}, \quad (17)$$

where i is the incidence angle and h is the flying height, gives equal significance to errors at the limit of resolution in either direction. The factor of 100 was chosen so that, if a joint adjustment of Mini-RF and optical images were performed, the errors in the two types of images would be approximately in balance. Residuals for optical imagers are measured in millimetres, which for a typical camera with a pixel spacing on the order of 10 μm results in a residual of 0.01 per pixel of error.

3.2 Processing Procedures

The USGS is developing the procedures for high-level radargrammetric processing of Mini-RF data, which will be used by team members at other institutions such as APL. This processing begins with importing the archived Level 1 data with PDS labels into ISIS by using the program *mrf2isis* and assigning trajectory data from a SPICE SPK file to the image with *spiceinit*. The file name of a DTM to be used for orthorectifying the data in ISIS can also be specified at this step if desired. Next, the program *fx* is used to calculate the desired type(s) of data from the four bands of the input cube. The Stokes S_1 parameter, which is the sum of the first two bands is generally used for stereo processing because it has the highest signal to noise ratio. S_1 and CPR are the quantities of greatest interest for mosaicking. These quantities may be normalized to a constant incidence angle by using *fx* to divide the data by an appropriate scattering model (Thompson et al. 2010) if desired. Scaling the S_1 data logarithmically (i.e., in decibels), again with *fx*, greatly improves the visibility of surface features compared to applying a linear stretch to 8 bit/pixel format. This log scaling is nearly essential for stereo processing and highly recommended for mosaic production.

For controlled mosaic production in ISIS, the programs *autoseed* and *pointreg* are used to automatically measure tiepoints between overlapping images, with candidate points distributed uniformly on a grid. The interactive program *qnet* is then used to check the validity of these feature matches and to add additional ties where needed (e.g. between images having opposite side viewing geometry, for which automated matching is less successful). A smaller number of ground control points are also needed for bundle adjustment, and are usually measured interactively by identifying features common to the images and to a base map such as laser altimetry data from Kaguya (Araki et al., 2009) or LOLA. The ISIS 3 tools for measuring ground

control are not yet as automated or fully integrated as those for image to image tiepoint determination. Once a sufficient set of measurements are obtained, the bundle adjustment is performed with *jigsaw* and the residuals are checked to identify erroneous measures. These bad measures are fixed or eliminated, and the process is repeated until a satisfactory control solution is obtained. The individual images are then orthorectified by using *cam2map* and mosaicked with *automos*.

For stereo processing in SOCET SET, the prepared Level 1 images and their trajectory data are exported by running *mrf4socet*. Once in SOCET SET, the Automatic and Interactive Point Measurement modules (APM/IPM) are used to gather the point measurements needed for bundle adjustment with Multi-Sensor Triangulation (MST). Collection of ground control is greatly facilitated because contours from the reference altimetry map can be overlaid on image pairs and viewed in stereo. Once the images are controlled, the Automatic Terrain Generation (ATG) module, and specifically the Next Generation Automatic Terrain Extraction algorithm (NGATE; Zhang, 2006) is used to produce a preliminary DTM by image matching. This can then be overlaid on the images in stereo, examined for errors, and edited with the Interactive Terrain Extraction (ITE) tools. When a satisfactory DTM is available, the images can be orthorectified. Finally, *ortho2isis3* and *dem2isis3* are used to export the orthoimages and DTM, respectively, to ISIS as Level 2 files.

4. QUALITY FACTORS AND TEST MAPPING

Our objectives in the work reported here were to test and refine the processing workflow described above, and to make at least preliminary estimates of the quality of the map products that could be produced by radargrammetric analysis of Mini-RF data in its most important geometric configurations. Before discussing the test mosaics and DTMs we have made, we first describe the main quality considerations and describe how they are likely to vary among the different image sets available. For controlled mosaics, the relevant measures of quality are the reduction of relative and absolute positional errors compared to uncontrolled products. These are likely to be limited by the precision of measurements on images and ground control, respectively, and are expected *a priori* to be comparable to (or ideally slightly less than) the pixel spacing of the images and the control DTM, respectively. The geometry of interest is that of the polar image sequences (cf. Figs. 1–3). These image sets have narrow overlaps between image strips from successive orbits, but also high-angle crossings where the images reach their maximum latitude and overlaps with opposite illumination where widely separated orbits cross. The latter will greatly strengthen the control of polar mosaics by directly linking distant images to one another. Image coverage of the equatorial zone (Fig. 4) is just beginning to be dense enough to support mosaic production. Equatorial mosaics would have only narrow overlaps between successive images and no cross-cutting high angle overlaps. Thus, relatively dense ground control would be required to maintain high absolute accuracy.

The main quality factors for DTMs are the horizontal resolution, which depends directly on the image resolutions, the expected vertical precision (EP) of height measurements, which depends on the stereo geometry as well as image resolutions, and absolute accuracy, which is a function of the bundle adjustment process in much the same way as for mosaic products. Horizontal resolution is limited by the minimum patch size compared in image matching. For optical images with high

signal to noise ratio, patches as small as 3x3 pixels can be used, leading to DTM resolutions as high as 3 times the image ground sample distance (GSD). The presence of speckle noise in SAR images is likely to necessitate larger matching areas and thus to reduce the achievable DTM resolution (Howington-Kraus, 2002; Kirk et al., 2010). The expected vertical precision can be estimated from the GSD (or the root mean square of the two image GSDs, if they differ), dimensionless stereo measurement error in pixels ρ , and the parallax-height ratio p/h :

$$EP = \rho GSD / (p/h). \quad (18)$$

As a rule of thumb, the factor ρ is often estimated as 0.2 pixel, and we have verified values close to this for optical images from a variety of planetary cameras. As with the horizontal resolution, the matching error for SAR is likely to be degraded by speckle noise and perhaps by the finite (2 or more pixels) resolution of the images. For the Cassini RADAR we estimate that ρ is on the order of 1 pixel, or about half the instrument resolution. For parallel image strips, the parallax-height ratio is given by (Leberl et al. 1992)

$$p/h = |\cot(i_1) \pm \cot(i_2)|, \quad (19)$$

where i_1, i_2 are the incidence angles of the two images. The plus sign applies for opposite-side viewing, which yields the best vertical precision, and the minus sign for same-side images, which will yield weaker or even nonexistent stereo if the incidence angles are similar. Pairs of images that cross at a high angle will have an intermediate p/h value but generally closer to the opposite-side case. Unfortunately, the active nature of radar imaging means that the greater the convergence angle between the two images, the greater the differences in illumination and thus in the appearance (shading) of slopes. Depending on the relative importance of intrinsic backscatter cross-section variations versus shading for a given target, opposite-look image pairs may be useful or may be almost impossible to match (Kirk et al., 2010). Incompatible illumination degrades the DTM quality less by increasing the error factor ρ for typical matched features than by increasing the fraction of the surface for which no acceptable match is obtained at all.

A further difficulty is that (just as for conventional aerial photographs) stereo convergence and stereo overlap are not independent for images taken at the standard off-nadir look angle. The polar mosaic sequences (Figs. 1–3) contain high-angle overlaps near the poles with relatively strong stereo but very limited areas, so that a large number of pairs would need to be used for mapping. At somewhat lower latitudes, adjacent images intersect at smaller angles, and as the degree of overlap increases to 100%, the convergence angle decreases to zero. Topographic mapping with such elongated and variable-quality image overlaps would also be challenging. The opposite-side overlaps are also elongated but have better and more consistent vertical precision. In the equatorial zone, there is little or no “incidental” stereo coverage obtained through the overlap of images with the standard look angle. An exciting prospect is the acquisition of deliberately targeted stereopairs with same-side viewing and different look angles. Although such imaging requires rotating the spacecraft for the second image of the pair, the results combine compatible same-side illumination, relatively strong stereo convergence, and full image overlap. Table 1 summarizes these considerations by providing *a priori* estimates of the horizontal resolution and vertical precision of various types of Mini-RF stereopairs. In these calculations, the useful DTM resolution is considered to be 7 pixels for same-

side image pairs and 15 pixels for opposite-side pairs, and $\rho=1$ pixel has been used throughout. Same-side images with identical look angles are assumed to overlap by 50%, all others by 100%.

Image Combination	Vertical Precision (m)	DTM resolution (m)	Swath width (km)
C-1 SS	500	500	6.5
C-1 OS	25	1000	13
C-1/LB SS	120	500	13
C-1/LZ SS	80	500	13
LB SS	500	500	9
LB OS	40	1000	18
LZ SS	50	50	9
LZ OS	4	100	18
LS SS targeted	60	500	15
LZ SS targeted	6	50	15

Table 1. Predicted quality factors for Mini-RF stereo DTMs. C-1 = Chandrayaan-1, LB = LRO baseline mode, LZ = LRO zoom mode, SS = same side, OS = opposite side.

From the table it is clear that LRO S-zoom mode imaging is highly preferred because of its greater resolution, and that targeted stereo observations are optimal, followed by opposite-side (or high angle) imaging. Our initial tests have therefore focused on precisely these types of image pairs.

4.1 LCROSS Impact Site in Cabeus Crater

The data for our initial mosaicking and DTM production tests come from the S-zoom imaging performed by LRO Mini-RF in support of LCROSS during its commissioning period (Neish et al., 2010). Images from orbits 455, 457, and 459 (east-looking, obtained on 1 August 2009) and 914, 920, and 922 (west-looking, obtained on 8–9 September 2009) were selected because they covered the predicted LCROSS impact point in the permanently shadowed interior of Cabeus (an 89-km diameter crater centered at 84.9°S, 35.5°E). In addition to being the LCROSS target, this area was of interest for controlled mosaic production because the uncontrolled mosaics of Vexel Level 2 images showed a substantial offset of 1.5 km between orbits 455 and 457, substantially exceeding the current estimated positional accuracy for LRO of ~100 m (Archinal et al., 2010).

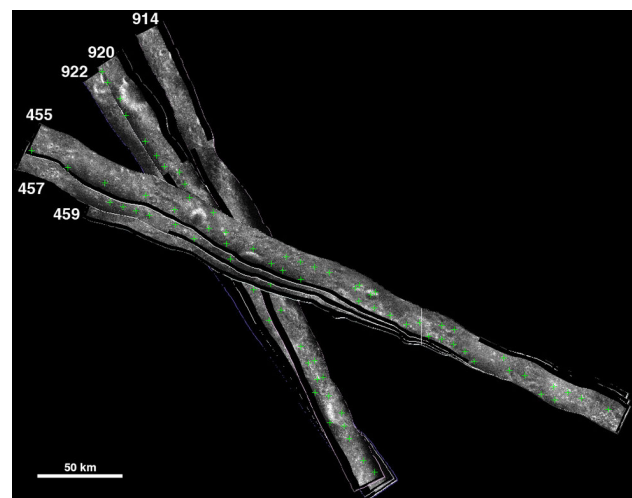


Figure 5. Mosaic of S-zoom images (labeled by orbit number) used to produce controlled mosaic of LCROSS impact site. Green crosses indicate image-to-image tiepoints obtained by automatic measurement.

Automated tie-point measurement in ISIS succeeded in generating a total of 65 tiepoints between successive (i.e., same-side illuminated) images as shown in Fig. 5, but did not yield ties between the two sets of orbits. Interactive measurements were used to define 11 tiepoints between the opposite-look image sets and 3 ground control points. Twelve tiepoints and one ground point were located within the area where the orbit swaths cross. A total of 205 image measurements were made. The ground points were constrained to elevations interpolated from Kaguya data gridded at 128 posts/degree (~240 m/post). This grid spacing—and more importantly the sparse distribution of actual measurements from which the Kaguya DTM was interpolated—was judged insufficient to refine the horizontal positioning of the images within their uncertainty, so the ground points were held to their *a priori* horizontal positions. The orbits were then bundle-adjusted with *jigsaw*. The root-mean-squared (RMS) residuals for the tie points dropped from 150 m to 12 m (1.6 pixels), with the maximum error decreasing from 900 m to 35 m. We produced two sets of mosaics in order to evaluate the relative positional errors visually: one uncontrolled and unrectified (projected onto the lunar reference sphere), and one based on the control adjustment and orthorectified with the Kaguya DTM. These products are compared in Figure 6. The uncontrolled mosaic shows a net offset of nearly 10 km between the two crossing orbit sets, mainly as a result of uncorrected stereo parallax. (This could be reduced by rectifying the uncontrolled images, but the results would contain additional local distortions caused by the misalignment of the images with the DTM.) This offset is reduced to the pixel level by adjustment and orthorectification. Parallax differences between the sequential orbits are much smaller, so the ~330 m offsets

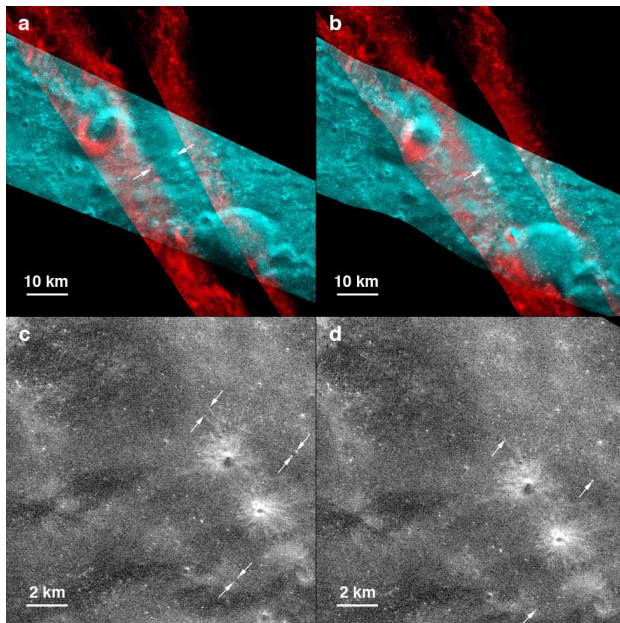


Figure 6. Comparison of uncontrolled and unrectified Mini-RF mosaics of LCROSS impact area (left) with controlled and rectified equivalents (right). (a) East- and west-looking images are shown in cyan and red, respectively to facilitate comparison. Note multi-kilometer offset between locations of the same crater (arrows). (b) As a, after control and rectification. Images of crater are now superimposed (arrow). (c) Uncontrolled mosaic of 400-series images enlarged to show offsets of ~300 m of corresponding features near the image seams (arrows). (d) As c, after control and rectification. Corresponding features now match at the single-pixel level (arrows). LCROSS impact point is located midway between the two prominent craters in c and d.

seen in the uncontrolled mosaic mainly reflect the errors in the *a priori* trajectory. Interestingly, we did not reproduce the 1500 m offset between orbits 455 and 457 in either our pre-adjustment residuals or in the uncontrolled mosaic, and its origin remains unexplained. In the controlled mosaic, orbit-to-orbit relative mismatches are reduced to the pixel level as implied by the adjustment residuals.

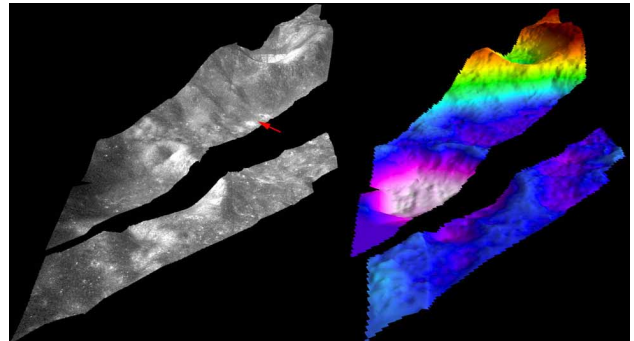


Figure 7. Simulated perspective views based on stereo DTM compiled from opposite-look pairs covering the vicinity of the LCROSS impact point (arrow). Area shown corresponds to the overlap area in Fig. 6 b and is viewed from the right side of that figure, with 2x vertical exaggeration. Left, DTM draped with orthorectified 400-series images. Right, shaded relief color-coded with elevation, from -5200 m (white) to 100 m (dark red).

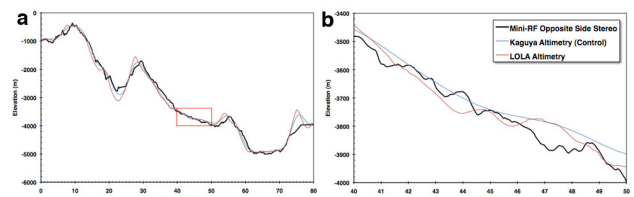


Figure 8. Profiles through the stereo DTM of the LCROSS impact area, compared to collocated Kaguya LALT and LRO LOLA altimetry data. (a) Profile runs from upper right to lower left as seen in Fig. 7. (b) Enlarged profile of region outlined by red box in a. Controlled stereo data are consistent with the altimetry at the level of tens of meters, but show numerous smaller details down to ~200 m in horizontal extent.

The six images used in the test mosaic were also imported into SOCET SET and independently controlled to the Kaguya DTM and bundle adjusted there. Interactive measurements were collected for 30 Z-Only points with elevations from Kaguya, plus 2 image-to-image tie points with unconstrained elevations. The overall RMS image residuals of the bundle adjustment was 1.636 pixels – comparable to the jigsaw results. We then collected DTM segments at 45 m/post by automatic matching of the nine opposite-look image pairs with NGATE. Matching was highly successful and only minimal editing of the DTM was required, mainly to address artifacts near the boundaries of the small DTM segments. The coverage gap in the middle of the DTM could be filled by analysis of same-side stereo. We performed stereomatching on the images from orbits 445 and 457. As expected because of the weaker stereo geometry, the result was much noisier than the opposite-side DTM segments and would require substantial manual editing. It is therefore not included in the figures shown here. Figure 7 shows perspective views of the combined DTM, both draped with the orthoimage and shown as a color-coded shaded relief map. Figure 8 compares a sample profile through the stereo DTM with collocated profiles from the ~240 m/post Kaguya and LOLA data sets. The stereo DTM set resolves features, down to about

200 m horizontally, many of which can be correlated with the images but are not seen in the altimetry. This approaches the resolution estimated in Table 1 and could probably be improved upon with further “tuning” of the matching algorithm parameters. The difference in resolution makes it difficult to estimate the vertical accuracy and precision of the DTM. Discrepancies between the profiles are clearly dominated by the topographic fluctuations in the stereo data rather than by systematic offsets, however, so the vertical accuracy of the controlled DTM can be estimated to be no worse than a few tens of meters. The amplitude of fluctuations in the stereo DTM approaches 10 m for the flattest areas on the floor of Cabeus. Since this is probably a mixture of real relief and stereo matching noise, 10 m is a reasonable bound on the vertical precision.

In the course of editing the Cabeus DTM we discovered a type of systematic error that we suspect has not been described previously because it is specific to planetary radar stereopairs: small impact craters appear to be elevated above their surroundings in opposite-look image pairs. This illusion is readily explained in terms of the intensity pattern of a crater surrounded by rough (therefore radar-bright) ejecta. If the two images of such a crater are correctly registered at the elevation of the crater rim, then the bright illuminated interior wall in one image corresponds with the dark wall in the other, and vice versa, leading to a low or even negative correlation. Shifting the images so that the bright wall in each image aligns with the bright exterior ejecta in the other, and so that the two dark walls coincide, will substantially increase the correlation between the two images. Unfortunately, this false correlation fools not only automated matching algorithms like NGATE, but also the human eye. When viewed in stereo, small craters appear to “float” above the surrounding terrain and closely match the erroneous surface contours produced by matching. Thus, it would be nearly impossible to remove the errors by interactive editing. A possible, though hardly ideal solution would be to filter the DTM to remove small elevated features up to some size threshold at which craters are correctly resolved, in the same way trees and buildings are filtered out of DTMs of Earth.

4.2 Jackson Crater

Our second radargrammetric test made use of a targeted stereo observation obtained on 25 April 2010. On orbit 3821, latitudes 7.5°S to 40°N near longitude 196°E were imaged with the normal off-nadir look angle, resulting in a centerline incidence angle of 44°–48°. On the following orbit, the same area was imaged at a reduced incidence angle of 24°–29°. Each observation was processed in four segments, corresponding to changes of the transmitted waveform and range gate needed to adapt to the changing target elevation. We restricted our processing to the first segment of each image, which covers the 71-km crater Jackson centered at 22.4°N, 196.9°E (Figure 9). Controlling the images in SOCET SET proved to be more difficult than for the Cabeus data set, because of substantial overall discrepancies in elevation between the stereo model and the LOLA DTM used as a control source. We resorted to a solution tied to LOLA by only a single well-defined ground point on the northern crater rim, with tie points distributed along the image strip. Adjustment residuals in the north-south along-strip direction could not be reduced below 2 pixels RMS, but this was sufficient for stereo matching to proceed very effectively, yielding a DTM at 25 m/post grid spacing. Only minor editing was required, again concentrated near the boundaries; the normalized editing time of ~0.8 hours per million DTM points compares favorably with HiRISE images

(Kirk et al., 2008b) and is dramatically less than required for Magellan or Cassini stereo data.

Comparison of the stereo DTM with the 128 posts/degree (~250 m/post) LOLA DTM for the same area revealed (in addition to dramatically greater detail in the stereo product) a very smooth discrepancy that varied almost quadratically with latitude. The latitudinal component of the adjustment residuals was also found to vary smoothly (in this case, as a cubic function) with latitude. The total variation of the north-south residuals was only ± 3 pixels (~45 m) but the elevation discrepancy varied by nearly 4000 m. Because the SOCET SET bundle adjustment module MST only permits first-order (i.e., position velocity bias) correction of the spacecraft trajectory, these offsets could not be removed by the adjustment. The ISIS adjustment program jigsaw allows higher-order corrections to the trajectory, so, with sufficient ground control, could probably adjust these images to remove the distortion. The cause of the extremely large trajectory error for one or both of these images has not yet been identified. Given the multi-km magnitude of the discrepancy, we are tempted to speculate that a gross error (such as using a predicted trajectory model instead of an actual reconstructed trajectory) was responsible.

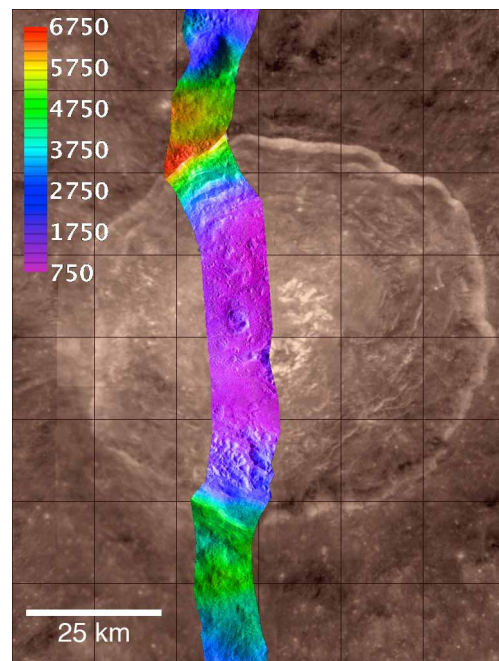


Figure 9. Orthorectified S-zoom image of part of Jackson crater, color-coded with elevation from targeted same-side stereopair. Stereo-derived elevations have been adjusted to match LOLA altimetry over distances >10 km, as described in text. Backdrop is Clementine UVVIS base mosaic, tinted brown to distinguish it from the radar imagery. Simple cylindrical projection, 195°–198°E, 20°–22°N.

Given these large errors in the *a priori* trajectory data, we cannot evaluate the level of absolute accuracy achieved in the controlled stereo DTM. The highly successful matching performance does confirm the expected benefits of targeted stereo observations, however, and examination of the DTM (Figure 10) reveals features as small as 50 m across. As with the Cabeus DTM, the correlation of many of these features with the images (e.g., the slump terraces on the crater rim) suggests that they are real and not merely due to errors in matching.

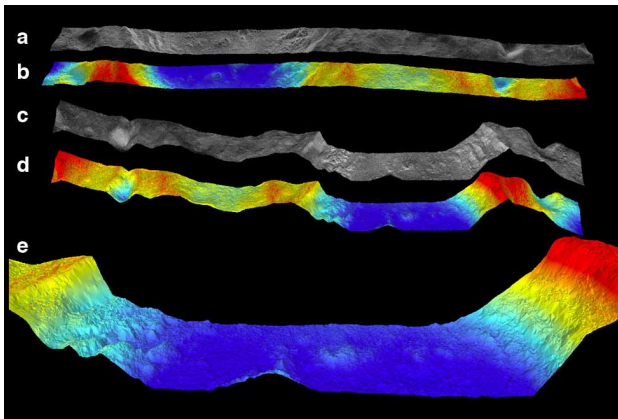


Figure 10. Perspective views of Jackson stereo DTM. (a) Draped with orthoimage, seen from west. (b) Shaded relief color-coded with elevation, seen from west. (c) As a, seen from east. (d) As b, seen from east. (e) Enlargement of d, showing detail on the crater floor of walls down to ~50 m horizontal scale. All views have 2x vertical exaggeration. The apparently greater relief of the views from the east is an artifact, caused by the deviation of the image edges where they follow the topography.

5. CONCLUSIONS AND FUTURE WORK

We have successfully developed and demonstrated a suite of radargrammetric tools that allow Mini-RF images to be bundle adjusted, orthorectified, and made into controlled mosaics in ISIS, and allow controlled DTMs to be produced by a combination of automated matching and interactive editing/quality control in SOCET SET. The ISIS tools will, in the near future, be released as part of the publically available (and free) ISIS system, allowing investigators worldwide to control, rectify, mosaic, and (with the many other tools that ISIS provides) analyze Mini-RF images at their home institutions. The topographic mapping capability requires SOCET SET software licenses and specialized hardware that may be too expensive for most researchers to justify, but roughly a dozen institutions are now using SOCET SET for planetary work with support from the USGS. In addition, the USGS/NASA Planetary Photogrammetry Guest Facility in Flagstaff (Kirk et al., 2009) provides free access to SOCET SET, including training, for qualified researchers. Thus, the tools we have developed should benefit a wide audience. These developments are timely, given that ~22 TB of Mini-RF data have already been archived in the NASA Planetary Data System, and the LRO instrument continues to acquire new images at a rate several orders of magnitude higher than originally planned. This includes collection of additional polar data, beginning in November 2010, and acquisition of ~50 image passes per year outside of the polar campaign. In the coming year, team members at the USGS and APL will work together to build control networks tying together the east- and west-looking sets of polar images, and will use the results to produce controlled and orthorectified mosaics of the poles. The team may eventually produce controlled mosaics in the equatorial zone if sufficient contiguous coverage is acquired.

Also in the near future, S-zoom targeted stereo observations of additional low-latitude areas will be acquired and used to produce DTMs. In addition to enabling detailed and quantitative morphological analyses of areas of high scientific interest, these DTMs will provide opportunities for us to further improve and assess our mapping techniques. Key goals include 1) identifying

(and if necessary taking steps to eliminate) the source of the large ephemeris errors seen at Jackson; 2) “tuning” the parameters of the automated stereo matching algorithm to optimize DTM resolution and minimize the number of errors needing editing, including testing a recent modification of the NGATE algorithm to improve its performance with SAR data and experimenting with matching CPR images (which have lower signal to noise ratio but are nearly independent of the illumination direction and thus could permit more accurate and unbiased matching for opposite-side image pairs); and 3) quantifying the DTM resolution and precision by comparison with higher resolution DTM data extracted from 0.5 m/pixel LROC images. The third goal would ideally be achieved by mapping one of the sites (Apollo 15 landing site and Tsiolkovskiy crater) at which the LROC team is comparing and documenting the quality of DTMs produced by different processing approaches (Beyer et al., 2010), but could be done with Mini-RF coverage of any of the tens of available LROC DTMs. As demonstrated by Kirk et al. (2008b) with HiRISE and HRSC images of Mars, a high resolution DTM in effect provides the “ground truth” without which full evaluation of the lower resolution DTM is nearly impossible. In any case, the results to date show that Mini-RF DTMs contain a great deal of geologically useful detail. Should LRO observation permit it, systematic acquisition of targeted stereo pairs covering as much as possible of the lunar equatorial zone would be highly desirable. The Mini-RF S-zoom images, which are intermediate between the LROC narrow- and wide-angle camera images in both resolution and swath width (Robinson et al., 2010), are nearly ideal for the task of filling the extensive multi-kilometer gaps between LOLA profiles near the equator with relatively high resolution stereo topographic data.

6. REFERENCES

- Acton, C.H., 1999. SPICE products available to the planetary science community. *Lunar Planet. Sci.*, XXX, Abstract #1233.
- Anderson, J.A., Sides, S.C., Soltesz, D.L., Sucharski, T.L., and Becker, K.J., 2004. Modernization of the Integrated Software for Imagers and Spectrometers. *Lunar Planet. Sci.*, XXXV, Abstract #2039.
- Araki, H., et al., 2009. Lunar Global Shape and Polar Topography Derived from Kaguya-LALT Laser Altimetry, *Science*, 323, 897–900, doi:10.1126/science.1164146.
- Archinal, B.A. et al., 2010. Tying LRO Data to the Fundamental Lunar Laser Ranging Reference Frame. *Lunar Planet. Sci.*, XLI, Abstract #2609.
- Batson, R.M., 1990. Cartography. In *Planetary Cartography* (R. Greeley and R.M. Batson, eds.), Cambridge Univ. Press., Cambridge, 60–95.
- Beyer, R. et al., 2010. LROC Stereo Data — Results of Initial Analysis. *Lunar Planet. Sci.*, Abstract #2678.
- Bussey, D.B.J. et al., 2003. Permanent shadow in simple craters near the lunar poles. *Geophys. Res. Lett.*, 30, 11-1, CiteID 1278, DOI 10.1029/2002GL016180.
- Campbell, B., 2002. *Radar Remote Sensing of Planetary Surfaces*. Cambridge University Press, Cambridge, 331 pp.
- Campbell, D.B., Campbell, B.A., Carter, L.M., Margot, J.-L., and Stacy, N.J.S., 2006. No evidence for thick deposits of ice at

- the lunar south pole. *Nature*, 443, 835–837, doi:10.1038/nature05167.
- Carter, L.M., et al., 2010. Mini-RF Observations of a Sample of Large Lunar Pyroclastic Deposits. *Lunar Planet. Sci.*, Abstract #1563.
- Colaprete, A., et al., 2009. An Overview of the Lunar Crater Observation and Sensing Satellite (LCROSS) Mission -- An ESMD Mission to Investigate Lunar Polar Hydrogen. *Lunar Planet. Sci.*, XL, Abstract #1861.
- Harmon, J.K., Perillat, P.J., and Slade, M.A., 2001. High-Resolution Radar Imaging of Mercury's North Pole. *Icarus*, 149, 1–15, doi:10.1006/icar.2000.6544.
- Howington-Kraus, E., Kirk, R., Galuszka, D., Hare, T., and Redding, B., 2002. Validation of the USGS Magellan sensor model for topographic mapping of Venus. *Lunar Planet. Sci.*, XXXIII, Abstract #1986.
- Kirk, R.L., Archinal, B.A., Gaddis, L.R., and Rosiek, M.R., 2008a. Cartography for lunar exploration: 2008 status and mission plans. *International Archives of Photogrammetry, Remote Sensing, and Spatial Information Sciences*, Beijing, China, XXXVII, Part 4, 1473–1480.
- Kirk, R.L., and Howington-Kraus, E., 2008. Radargrammetry on three planets. *International Archives of Photogrammetry, Remote Sensing, and Spatial Information Sciences*, Beijing, China, XXXVII, Part 4, 973–980.
- Kirk, R.L., Howington-Kraus, E., and Rosiek, M.R., 2009. Build Your Own Topographic Model: A Photogrammetry Guest Facility for Planetary Researchers. *Lunar Planet. Sci.*, XL, Abstract #1414.
- Kirk, R.L., et al., 2008b. Ultrahigh resolution topographic mapping of Mars with MRO HiRISE stereo images: Meter-scale slopes of candidate Phoenix landing sites. *J. Geophys. Res.*, 113, E00A24, doi:10.1029/2007JE003000.
- Kirk, R.L. et al., 2010. Three-Dimensional Views of Titan's Diverse Surface Features from Cassini RADAR Stereogrammetry. *Icarus*, in revision.
- Leberl, F.W., Thomas, J.K., and Maurice, K.E., 1992b. Initial results from the Magellan Stereo Experiment. *J. Geophys. Res.* 97(E8), 13,675–13,689.
- Miller, S.B., and Walker, A.S., 1993. Further developments of Leica digital photogrammetric systems by Helava. *ACSM/ASPRS Annual Conv.* 3, 256–263.
- Miller, S.B., and Walker, A.S., 1995. Die Entwicklung der digitalen photogrammetrischen Systeme von Leica und Helava. *Z. Phot. Fern.* 63(1), 4–16.
- Neish, C.D., Bussey, D.B.J., Spudis, P., Marshall, W., Thomson, B., Patterson, G.W., Carter, L., and the Mini-RF Science Team, 2010. The nature of lunar volatiles as revealed by Mini-RF observations of the LCROSS impact site. *J. Geophys. Res.*, in review.
- Nozette, S. et al., 2010. The Lunar Reconnaissance Orbiter Miniature Radio Frequency (Mini-RF) Technology Demonstration. *Space Sci. Rev.*, 150, 285–302, doi:10.1007/s11214-009-9607-5.
- Nozette, S., C. Lichtenberg, P. D. Spudis, R. Bonner, W. Ort, E. Malaret, M. Robinson, and E. M. Shoemaker, 1996. The Clementine bistatic radar experiment. *Science*, 274, 1495–1498, doi:10.1126/science.274.5292.1495.
- Nozette, S., E. M. Shoemaker, P. D. Spudis, and C. L. Lichtenberg, 1997. The possibility of ice on the Moon. *Science*, 278, 144–145, doi:10.1126/science.278.5335.144.
- Raney, R. K., 2007. Hybrid-polarity SAR architecture. *IEEE Trans. Geosci. Remote Sens.*, 45, 3397–3404, doi:10.1109/TGRS.2007.895883.
- Reid, M., 2010. SIS For Mini-RF Advanced Technologies Lunar Reconnaissance Orbiter (LRO) Payload Operations Center. Document MRF-4009, version February 25, 2010. http://pds-geosciences.wustl.edu/lro-mini-rf-1/lro-l-mrflro-4-cdr-v1/lromrf_0001/document/dp_sis/mrflro_dp_sis.pdf (accessed 9 Sep. 2010).
- Robinson, M.S., et al., 2010. Lunar Reconnaissance Orbiter Camera (LROC) Instrument Overview. *Space Sci. Rev.*, 150, 81–124, doi:10.1007/s11214-010-9634-2.
- Smith, D.E. et al., 2010. The Lunar Orbiter Laser Altimeter Investigation on the Lunar Reconnaissance Orbiter Mission. *Space Sci. Rev.*, 150, 209–241, doi:10.1007/s11214-009-9512-y.
- Spudis, P.D., et al., 2010. Initial results for the north pole of the Moon from Mini-SAR, Chandrayaan-1 mission. *Geophys. Res. Lett.*, 37, L06204, doi:10.1029/2009GL042259.
- Thompson, T.W., Ustinov, E.A., and Heggy, E., 2010. Modeling Radar Scattering from Icy Lunar Regoliths. at 13-cm and 4-cm Wavelengths. *J. Geophys. Res.*, in press.
- Thomson, B.J., Spudis, P.D., Bussey, D.B.J., Carter, L., Kirk, R.L., Neish, C., Patterson, G., Raney, R.K., Winters, H., and the Mini-RF Team, 2010. Roughness and radar polarimetry of lunar polar craters: Testing for ice deposits. *Lunar Planet. Sci.*, XLI, Abstract #2176.
- Trang, D. et al., 2010. Using Mini-RF to Investigate the Anomalous UVVIS Spectrum in the Apollo and Plato Region. *Lunar Planet. Sci.*, XLI, Abstract #2652.
- Zhang, B., 2006. Towards a higher level of automation in softcopy photogrammetry: NGATE and LIDAR processing in SOCET SET®. *GeoCue Corporation 2nd Annual Technical Exchange Conference*, Nashville, Tennessee, 26–27 September, 32 pp.